
S³GNN: Efficient Global Mixing and Local Message Passing for Long-Range Graph Learning

Dai Shi^{*1} Luke Thompson^{*2} Linhan Luo^{*2} Lequan Lin² Andi Han²
 Junbin Gao² José Miguel Hernández Lobato¹

Abstract

Message-passing neural networks (MPNNs) often suffer from an information bottleneck when capturing long-range dependencies, leading to the oversquashing (OSQ) phenomenon. Alongside spatial connectivity enrichment (e.g., rewiring), recent studies have shown that spectral filtering can yield strong long-range learning outcomes, as spectral operators enable global information mixing that alleviates OSQ. These approaches achieve this either by stabilizing the Jacobian energies in deep propagation or by guaranteeing OSQ mitigation under strong theoretical assumptions. We revisit these conclusions and show that the associated Jacobian sensitivity lower bound is generally difficult to achieve in practice. We then propose S³GNN, which mitigates OSQ without such restrictive assumptions by lightweightly reintroducing omitted components with substantially lower computational complexity, while standard stability constraints on feature transformations remain effective under our new dynamics. Extensive experiments across diverse domains (e.g., long-range benchmarks, KGQA, and mesh-based fluid dynamics) demonstrate that S³GNN achieves up to an order-of-magnitude error reduction with up to 50% fewer parameters. Our code can be found in <https://github.com/EEthanShi/S3-GNN.git>.

1. Introduction

Graph neural networks (GNNs) have emerged as the fundamental deep learning models for handling graph-structured data (Wu et al., 2020; Ji et al., 2021; Sato, 2020; Rusch et al.,

¹Department of Engineering, University of Cambridge, Cambridge, UK. ²University of Sydney, Australia.. Correspondence to: Dai Shi <ds2213@cam.ac.uk>.

Proceedings of the 43rd International Conference on Machine Learning, Seoul, South Korea. PMLR 306, 2026. Copyright 2026 by the author(s).

2023). The oversquashing phenomenon, one of the recently identified problems within GNN dynamics (Shi et al., 2023; Topping et al., 2021; Alon & Yahav, 2020), refers to the degradation of learning outcomes when information from distant nodes cannot be effectively communicated through limited message-passing channels, causing long-range dependencies to be compressed and lost in feature propagations. The mainstream of the research in mitigating the OSQ problem refers to the rewiring techniques, which enrich the graph connectivity based on some graph indicators, such as curvature (Topping et al., 2021; Fesser et al., 2023; Nguyen et al., 2023) and spectral gap (Black et al., 2023; Deac et al., 2022; Karhadkar et al., 2023), to name a few.

Rather than spatially enriching graph connectivity, recent studies (Geisler et al., 2024; Hariri et al., 2025) have illustrated the potential of resolving OSQ with the help of spectral filtering due to its advantage of providing global long-range information. Such spectral methods have achieved excellent performance by (i) stabilizing the weight matrices to prevent vanishing/exploding Jacobian energies in depth, as in Hariri et al. (2025), or by (ii) combining spatial and spectral dynamics, where the theoretical guarantees for OSQ mitigation typically rely on strong conditions (Geisler et al., 2024).

In this paper, we revisit the OSQ vanishing analysis in (Geisler et al., 2024) and verify that the corresponding theoretical lower bound is *difficult to attain* in practice. We then demonstrate that effective alleviation of OSQ can still be achieved after relaxing these restrictive conditions, by carefully reintroducing previously omitted model components in a lightweight manner with *significantly lower computational complexity*. Finally, we incorporate stability constraints on the feature transformation into our new model and show that such constraints continue to play a stabilizing role on the Jacobian energy, thereby yielding a simple yet effective architecture for mitigating OSQ in practice. We summarize our contributions as follows.

- **Identification on the gap between theory and practice.** We revisit the OSQ-vanishing analysis of the spectral GNNs, e.g., (Geisler et al., 2024) and show that the associated theoretical lower bound is difficult

to attain under practical implementations.

- A lightweight global-mixing dynamics with non-vanishing influence.** We propose S³GNN, which reintroduces spatial propagation and a simple feature transform on top of a low-rank global mixing term, enabling efficient global information exchange with per-layer complexity comparable to GCN and *without expensive eigendecomposition*; although motivated by spectral filtering, our model is implemented entirely in the spatial domain and admits a distance-independent non-vanishing influence lower bound.
- Stabilized propagation via constrained feature transforms.** Inspired by stability-constrained spectral GNNs, we incorporate antisymmetric constraints on the feature transformation and show that the resulting Jacobian energy is still stable in our proposed model, yielding a simple yet effective OSQ-mitigating architecture.
- Strong empirical performance with reduced cost.** We evaluate our proposed model via massive experiments. Our model achieves *orders-of-magnitude* better results in both synthetic and real-world datasets with cheaper computational costs. Furthermore, we also show that our model can be a strong backbone model in multiple situations, such as knowledge graph question answering (KGQA), topological interpolation, and fluid dynamics prediction.

2. Background

In this work, we denote a graph as a tuple $\mathcal{G} = (\mathcal{V}, \mathcal{E})$ where \mathcal{V} and \mathcal{E} denote the set of N nodes and m edges, respectively. In most cases, we assume that \mathcal{G} is undirected, i.e., if $(i, j) \in \mathcal{E}$, then $(j, i) \in \mathcal{E}$. We let $\mathbf{A} \in \mathbb{R}^{N \times N}$ be the unweighted adjacency matrix, and the normalized adjacency matrix is denoted by $\widehat{\mathbf{A}} = \mathbf{D}^{-1/2} \mathbf{A} \mathbf{D}^{-1/2}$ where \mathbf{D} is the degree matrix. We further define $\mathbf{L} \in \mathbb{R}^{N \times N}$ as the graph Laplacian matrix with $\mathbf{L} = \mathbf{D} - \mathbf{A}$. Accordingly, the normalized graph Laplacian is given by $\widehat{\mathbf{L}} = \mathbf{I} - \widehat{\mathbf{A}}$, and has eigendecomposition such that $\widehat{\mathbf{L}} = \mathbf{U} \mathbf{\Lambda} \mathbf{U}^\top$. In this paper, we let $\{(\lambda_i, \mathbf{u}_i)\}_{i=1}^N$ be the set of eigenvalue and eigenvector pairs of $\widehat{\mathbf{L}}$. Finally, A connected component of \mathcal{G} is a maximal subset of nodes $\mathcal{C} \subseteq \mathcal{V}$ such that any two nodes in \mathcal{C} are connected by a path in \mathcal{G} . Suppose \mathcal{G} has k connected components $\{\mathcal{C}_r\}_{r=1}^k$ with $|\mathcal{C}_r| = n_r$. It is well known that for unnormalized Laplacian \mathbf{L} , the eigenvalue 0 has multiplicity k , and a orthonormal basis of the 0-eigenspace is given by $\{\mathbf{v}^{(r)}\}_{r=1}^k$, where $(\mathbf{v}^{(r)})_i = \frac{1}{\sqrt{n_r}}$ if $i \in \mathcal{C}_r$, and 0 otherwise.

2.1. Graph Neural Networks

In general, there are two types of GNNs. Spatial message passing neural networks (MPNNs) propagate node features by gathering their *local* neighboring information (Gilmer et al., 2017), resulting in the following dynamic

$$\mathbf{h}_i(\ell + 1) = \phi_\ell(\mathbf{h}_i(\ell), \sum_{j \in \mathcal{N}_i} \widehat{\mathbf{A}}_{ij} \psi_\ell(\mathbf{h}_i(\ell), \mathbf{h}_j(\ell))), \quad (1)$$

where $\mathbf{h}_i(\ell)$ represents the feature of node i at layer ℓ , with $\mathbf{h}_i(0) = \mathbf{x}_i$, and $\psi_\ell : \mathbb{R}^{d_\ell} \times \mathbb{R}^{d_\ell} \rightarrow \mathbb{R}^{d_\ell}$, $\phi_\ell : \mathbb{R}^{d_\ell} \times \mathbb{R}^{d_\ell} \rightarrow \mathbb{R}^{d_{\ell+1}}$ are channel-mixing and update functions, respectively. One typical example of MPNN is GCN and its variants (Kipf & Welling, 2017), with the dynamic defined as $\mathbf{H}(\ell + 1) = \sigma(\widehat{\mathbf{A}} \mathbf{H}(\ell) \mathbf{W}(\ell))$. Another routine of GNN is to conduct feature propagation through *global* spectral filtering on the eigenspace of \mathbf{L} . That is

$$\mathbf{H}(\ell + 1) = \mathbf{U}(g_\theta(\mathbf{\Lambda})) \mathbf{U}^\top \mathbf{H}(\ell) \mathbf{W}(\ell), \quad (2)$$

where $g_\theta(\cdot) : \mathbb{R} \rightarrow \mathbb{R}$ is the learnable spectral filtering function parameterized by θ , and $g_\theta(\mathbf{\Lambda}) = \text{diag}(g_\theta(\lambda_i))$. To avoid the $\mathcal{O}(N^3)$ eigendecomposition in Eq. (2), the ChebNet in (Defferrard et al., 2016) uses $\mathbf{U} g_\theta(\mathbf{\Lambda}) \mathbf{U}^\top \mathbf{H} \approx \sum_{p=0}^K \beta_p T_p(\tilde{\mathbf{L}}) \mathbf{H}$, where $T_p(\cdot)$ denotes the Chebyshev polynomial of degree p , $\{\beta_p\}_{p=0}^K$ are the learnable Chebyshev coefficients, and $\tilde{\mathbf{L}} := \frac{2}{\lambda_{\max}} \mathbf{L} - \mathbf{I}$ is the rescaled Laplacian (with λ_{\max} the largest eigenvalue of \mathbf{L}).

2.2. Oversquashing in GNNs

OSQ was first characterized as an information bottleneck in message passing (Alon & Yahav, 2020) and later quantified via the Jacobian sensitivity score (Topping et al., 2021):

$$\text{OSQ}^{(\ell)}(i, s) = \left\| \frac{\partial \mathbf{h}_i(\ell)}{\partial \mathbf{x}_s} \right\|, \quad (3)$$

which typically decays rapidly with depth ℓ , limiting long-range communication and degrading performance on tasks that rely on distant interactions (Shi et al., 2023). Motivated by their global filtering behavior, spectral GNNs such as ChebNet (Defferrard et al., 2016), Stable-ChebNet (Hariri et al., 2025), and S²GNN (Geisler et al., 2024) have recently shown strong performance on long-range benchmarks. In particular, Stable-ChebNet follows

$$\mathbf{H}(\ell + 1) = \mathbf{H}(\ell) + \epsilon \sum_{p=0}^K T_p(\tilde{\mathbf{L}}) \mathbf{H}(\ell) \widehat{\mathbf{W}}_p(\ell), \quad (4)$$

where $\epsilon > 0$ is the step size and $\widehat{\mathbf{W}}_p(\ell)$ is antisymmetric, i.e., $-\widehat{\mathbf{W}}_p(\ell) = \widehat{\mathbf{W}}_p^\top(\ell)$. The dynamic of S²GNN can be written as

$$\mathbf{H}(\ell + 1) = \mathbf{U} \left(g_\theta^{(\ell)}(\mathbf{\Lambda}) \odot \left[\mathbf{U}^\top f_\theta^{(\ell)}(\mathbf{H}(\ell)) \right] \right) + \widehat{\mathbf{A}} \mathbf{H}(\ell) \mathbf{W}(\ell), \quad (5)$$

where \odot denotes the element-wise product and $f_{\tilde{\theta}}^{(\ell)} : \mathbb{R}^{N \times d_\ell} \rightarrow \mathbb{R}^{N \times d_\ell}$ is a feature transformation function. We conduct a literature review on the MPNN methods for mitigating the OSQ problem in the Appendix A.

3. Method

3.1. Gap Between Theory and Practice

In this section, we show how our S³GNN model is designed. Based on the description of the OSQ problem aforementioned, to ensure an effective *information transaction* between node pairs (so that the OSQ problem can be diminished), the GNN dynamic shall possess a positive lower bound, i.e., $\left\| \frac{\partial \mathbf{h}_i(\ell)}{\partial \mathbf{x}_s} \right\| > 0$ for any layer ℓ . Although remarkable conclusions have been explored by delivering upper bounds of $\left\| \frac{\partial \mathbf{h}_i(\ell)}{\partial \mathbf{x}_s} \right\|$ via different dynamics and rewiring methods (Topping et al., 2021; Banerjee et al., 2022; Black et al., 2023), a lower bound is only presented for the dynamic of S²GNN described in Eq. (5). Specifically, consider the dynamic in Eq. (5): if one sets (i) $f_{\tilde{\theta}}^{(\ell)} = \text{id}$; (ii) $\hat{\mathbf{A}}\mathbf{H}(\ell)\mathbf{W}(\ell) = 0$; (iii) chooses the spectral filter such that $g_{\theta}^{(\ell)}(\lambda) = C(\theta) > 0$ when $\lambda = 0$, and $g_{\theta}^{(\ell)}(\lambda) = 0$ when $\lambda > 0$, where $C(\theta)$ is the positive filtering coefficient determined by the model parameters, then for any $i, s \in \mathcal{C}_r$, we have the lower bound as

$$\left\| \frac{\partial \mathbf{h}_i(\ell)}{\partial \mathbf{x}_s} \right\| \geq \frac{C^\ell(\theta)}{2|\mathcal{E}_{\mathcal{C}_r}|}, \quad (6)$$

where $|\mathcal{E}_{\mathcal{C}_r}|$ is the number of edges in \mathcal{C}_r ¹. One can check that under assumptions (i)-(iii), the S²GNN dynamic becomes the simple diagonal spectral filtering dynamic

$$\begin{aligned} \mathbf{H}(\ell + 1) &= \mathbf{U} \text{diag}(g_{\theta}^{(\ell)}(\mathbf{\Lambda})) \mathbf{U}^\top \mathbf{H}(\ell) \\ &= C(\theta) \mathbf{U} \text{diag}(\mathbf{1}_{\{\lambda_i=0\}}) \mathbf{U}^\top \mathbf{H}(\ell), \end{aligned} \quad (7)$$

which is substantially different from the concrete implementation of S²GNN in Eq. (5). Accordingly, one may want to exploit the following question.

Can S²GNN really exceed the theoretical lower bound in Eq. (6) if its concrete dynamic is that of Eq. (5)?

In this spirit, we test the dynamics in Eq. (5) and Eq. (7) in *peptides-struct* dataset, a gold-standard long-range graph benchmarks (Dwivedi et al., 2022). Both models are trained via the MAE loss, with the Jacobian norms computed prior to the global pooling layer. We note that given most of the graphs in *peptides-struct* are connected, yielding there is only one 0-eigenvalue to be filtered in Eq. (7). Accordingly,

¹We note that the original lower bound in (Geisler et al., 2024) is defined via entry-wise 1-norm (Theorem 2). Since $\|\cdot\|_2 \geq \frac{1}{d} \|\cdot\|_{L_1}$ for any $d \times d$ matrix, we have Eq. (6).

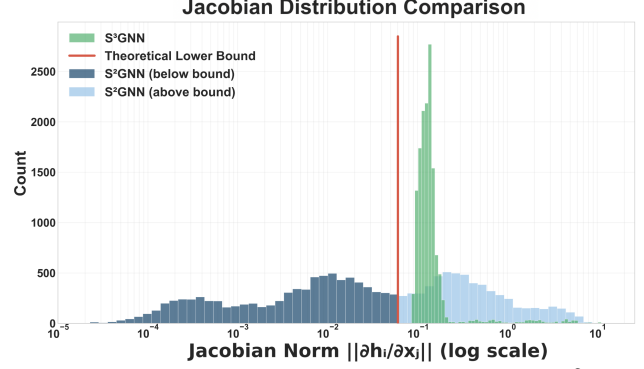


Figure 1. Jacobian norm distribution comparison between S²GNN, diagonal filtering in Eq. (7), and our proposed S³GNN.

in the non-normalized Laplacian setting, one can verify that $\left\| \frac{\partial \mathbf{h}_i(\ell)}{\partial \mathbf{x}_s} \right\| = \frac{C^\ell(\theta)}{2N}$, i.e., a constant. We followed exact hyperparameter settings for S²GNN, yielding test MAE over 5 runs as 0.2487 ± 0.0019 (33.5s per epoch) and 0.6824 ± 0.0149 (0.46s per epoch) for dynamics in Eq. (7). The Jacobian norm distribution (log scale) of one test graph sample (more examples are in Appendix C.1) is shown in Figure 1. We observe many more **below-bound values** than **above-bound values**, suggesting a violation between theory in the ideal situation and real practice, where the *computational complexity* is much higher. For example, for implementing Eq. (5), rather than conducting simple diagonal filtering like in Eq. (7), g_{θ} is parameterized by the composition of Gaussian smearing and linear transformation on a specific spectral truncation (approximately 70% of $\mathbf{\Lambda}$ from lowest), and the feature transformation $f_{\tilde{\theta}}$ is usually implemented with a non-linear gating mechanism.

3.2. Lightweight Global Mixing with Non-Vanishing Influence

Having observed the phenomenon in Section 3.1, it is natural for us to explore the following.

Can one maintain the advantage in Eq. (7) for the OSQ problem, while reintroducing the sacrificed components with significantly lower complexity?

Accordingly, we consider the following continuous-time dynamics.

$$\frac{\partial \mathbf{H}(t)}{\partial t} = \mathbf{U} \text{diag}(g_{\theta}^{(t)}(\mathbf{\Lambda})) \mathbf{U}^\top \mathbf{H}(t) \mathbf{W}(t) + \hat{\mathbf{A}} \mathbf{H}(t) \mathbf{W}(t), \quad (8)$$

where we reintroduce simple feature transformation to a *linear* map, $f_{\tilde{\theta}}(\mathbf{H}) = \mathbf{H} \mathbf{W}_{\tilde{\theta}}$, and keep the spatial part in the model dynamics. In addition, we maintain $g_{\theta}(\lambda) = 0$ for $\lambda > 0$ as in Eq. (7). Applying the forward Euler scheme with step size ϵ yields the discrete update $\mathbf{H}(\ell + 1) = \mathbf{H}(\ell) + \epsilon \left(\mathbf{U} \text{diag}(g_{\theta}^{(\ell)}(\mathbf{\Lambda})) \mathbf{U}^\top \mathbf{H}(\ell) \mathbf{W}(\ell) + \hat{\mathbf{A}} \mathbf{H}(\ell) \mathbf{W}(\ell) \right)$.

$\widehat{\mathbf{A}}\mathbf{H}(\ell)\mathbf{W}(\ell)$). One can check that this dynamic substantially reduces the computational cost in S^2GNN . In addition, one can write $\mathbf{P}_\theta = \mathbf{U}\text{diag}(g_\theta(\mathbf{\Lambda}))\mathbf{U}^\top = \sum_{r=1}^k \alpha_{\theta,r} \mathbf{v}^{(r)}\mathbf{v}^{(r)\top}$, where $\{\mathbf{v}^{(r)}\}_{r=1}^k$ are the orthonormal basis vectors of the 0-eigenspace of \mathbf{L} , and $(\mathbf{v}^{(r)}\mathbf{v}^{(r)\top})_{ij} = 1/n_r$ for $i, j \in \mathcal{C}_r$ and 0 otherwise. Therefore, the propagation can be implemented **without computing eigendecomposition**. As a result, each layer only involves (i) a *sparse neighborhood aggregation*, and (ii) a *low-rank global mixing*, resulting in

$$\mathbf{H}(\ell+1) = \mathbf{H}(\ell) + \epsilon \left(\mathbf{P}_\theta(\ell)\mathbf{H}(\ell)\mathbf{W}(\ell) + \widehat{\mathbf{A}}\mathbf{H}(\ell)\mathbf{W}(\ell) \right), \quad (9)$$

which shows the computational complexity of the dynamic comparable to classic GCNs. More importantly, for each connected component \mathcal{C}_r , one may consider \mathbf{P}_θ as adding a *scalar-reweighted fully-connected* subgraph, and this setting ensures *effective information transaction* within each connected component. This aligns with the spirit of methods which densify graph connectivity through rewiring (Topping et al., 2021) and graph transformers (Wu et al., 2023b) in mitigating OSQ. Formally, one can derive the following conclusion (proof in Appendix).

Proposition 1 (Non-vanishing influence (existence direction)). *Consider the dynamics in Eq. (9). Fix a connected component \mathcal{C}_r with $|\mathcal{C}_r| = n_r$. Assume that the feature transform $\mathbf{W}(\ell) \in \mathbb{R}^{d \times d}$ is non-degenerate, i.e., $\sigma_{\min}(\mathbf{W}(\ell)) > 0 \forall \ell$, and that the mixing coefficient satisfies $\alpha_{\theta,r}^{(\ell)} > 0$. Then for any $i, s \in \mathcal{C}_r$, layer number ℓ such that*

$$\left\| \frac{\partial \mathbf{h}_i(\ell)}{\partial \mathbf{x}_s} \right\| \geq \prod_{p=0}^{\ell-1} \left(\epsilon \frac{\alpha_{\theta,r}^{(p)}}{n_r} \sigma_{\min}(\mathbf{W}(p)) \right). \quad (10)$$

In particular, the lower bound is independent of the graph distance between i and s within \mathcal{C}_r .

Proposition 1 further indicates that to engage long-range communication between nodes when it is highly needed, one may expect to have $\alpha_{\theta,r} > 0$ and larger when ℓ goes higher. We frequently observe this phenomenon in our numerical experiments, e.g., see more results in Figure. 3.

3.3. Jacobian Stability and Flexible Choice of Feature Transformation

With the increase of layers, the dynamics can become increasingly unstable, without properly constraining the weights. Specifically, the dynamics in Eq. (9) can suffer from the unstable Jacobian energy in each layer (Hariri et al., 2025). To see this, one can let $\mathbf{J}(\ell) = \frac{\partial \text{vec}(\mathbf{H}(\ell+1))}{\partial \text{vec}(\mathbf{H}(\ell))} \in \mathbb{R}^{Nd \times Nd}$ (assume \mathcal{G} is connected for simplicity), so that

the Jacobian energy of each ℓ can be denoted as $\|\mathbf{J}(\ell)\|_2$. Motivated by the Stable-ChebNet (Hariri et al., 2025), we incorporate antisymmetric constraint on \mathbf{W} , resulting in

$$\mathbf{H}(\ell+1) = \mathbf{H}(\ell) + \epsilon \left(\mathbf{P}_\theta(\ell)\mathbf{H}(\ell)\widehat{\mathbf{W}}(\ell) + \widehat{\mathbf{A}}\mathbf{H}(\ell)\widehat{\mathbf{W}}(\ell) \right), \quad (11)$$

where $\widehat{\mathbf{W}}$ satisfies the antisymmetric property as Eq. (4). In practice, one can deploy two antisymmetric matrices, with each corresponding to the global-mixing and spatial part. As our model was originally motivated by S^2GNN (Geisler et al., 2024), but with simpler and stability guarantee (See proposition 2 below), we therefore name our model as S^3GNN , and we show the stability guarantee as follows.

Proposition 2 (Stability). *The Jacobian energy of S^3GNN in Eq. (11) is stable, i.e., no exponential growth or decay in each layer. That is $\|\mathbf{J}(\ell)\|_2 = 1 + \mathcal{O}(\epsilon^2)$.*

Figure 2 visualizes the propagation of our S^3GNN on the Barbell graph, a synthetic node-level regression task for testing OSQ robustness (Bamberger et al., 2025; Hariri et al., 2025). In addition, we show comparisons in MSE loss and number of parameters between our model and Stable-ChebNet. Our key observations are

1. S^3GNN delivers **orders-of-magnitude** better MSE with much **fewer parameters**. For example, our model is around 30 times better in the case when $N = 50$ compared to Stable-ChebNet, i.e., 0.17 V.S 0.005, whilst halving the number of parameters, i.e., 262K V.S 591K.
2. Our model achieves this remarkable result with only 4 layers compared to ChebNet and Stable-ChebNet, in which the polynomial order is up to 10 with 4 layers, suggesting a **more effective information transaction**.
3. When parameter count is matched (i.e., 657K), S^3GNN maintains leading performances across domains, supporting the effectiveness of incorporating antisymmetric feature transformation in our model.

Lastly, we also present the Jacobian norm distribution of S^3GNN results (MAE = 0.2429±0.0014) in Figure 1, and one can observe that all values in **green** are beyond the theoretical lower bound. This directly verifies that the elements that S^3GNN leveraged additional to the diagonal spectral filtering dynamic in Eq. (5) indeed improve the long-range communication between distant nodes from both theory (i.e., Proposition 1) and practical sides.

Flexible Choice of Feature Transform In our proposed S^3GNN , we constrain $\widehat{\mathbf{W}}$ to be antisymmetric to stabilise the Jacobian energy, $\|\mathbf{J}(\ell)\|_2$. However, the choice of feature transformation can be varied. For example, based on

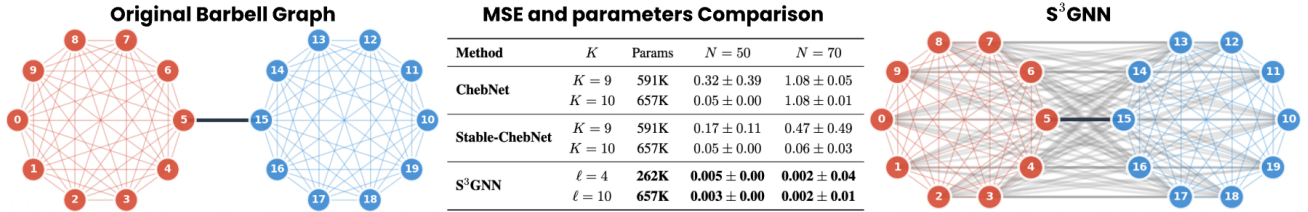


Figure 2. Illustration on S³GNN dynamic, i.e., neighborhood aggregation and global mixing in Barbell graph, and comparison between S³GNN with spectral methods, e.g., ChebNet and Stable-ChebNet in terms of learning accuracy and number of parameters. Our S³GNN show order-of-magnitude better performances with less parameters.

Proposition 1, one may let \mathbf{W} be orthogonal matrix, so that $\sigma_{\min} = 1$ to eliminate the effect of \mathbf{W} in Eq. (10). From a geometric viewpoint, such an orthogonality requirement can be understood as a manifold constraint that restricts \mathbf{W} to lie on the orthogonal group, thereby enforcing norm-preserving feature transport across layers. In addition, inspired by manifold-constrained mixing mechanisms in deep residual architectures (Xie et al., 2025; Mishra, 2026; Shi et al., 2021), one may also consider using doubly stochastic transforms to mix feature channels while preserving simple aggregate quantities (e.g., keeping the per-layer feature mean unchanged). We explore this further in Section 4.6.

4. Experiments

We evaluate our S³GNN in multiple tasks, such as graph-level property prediction, large-scale node classification (both in Section 4.1), long-range graph benchmarks (Section 4.2), multi-hop/entity KGQA (Section 4.3), topological interpolation (Section 4.4), and mesh-based fluid dynamics prediction (Section 4.5). In addition, we also conduct ablation studies and provide a discussion on future research directions in Section 4.6. Additional experiments (e.g., on heterophily graphs) and comparisons are included in the Appendix. All experiments are executed on an NVIDIA[®] H200 SXM GPU (141 GB HBM3e) within an HPC cluster.

4.1. Graph Property Prediction Dataset

We first evaluate the performance of S³GNN via the graph property prediction dataset provided by (Corso et al., 2020) followed by the experiment settings in (Gravina et al., 2022; Hariri et al., 2025). The dataset consists of undirected graphs sampled from a diverse collection of random and structured graph families (e.g., Erdős-Rényi, Barabási-Albert, and caterpillar graphs), thereby covering a wide range of topological properties. Followed by (Gravina et al., 2022), the node number in each graph is between 25 and 35 to increase the task complexity and raising the need for long-range information propagation. Specifically, *Diameter* is a graph-level regression task, whereas *Single Source Shortest Path (SSSP)* and *Eccentricity* are node-level regression tasks, respectively. In addition, as S³GNN provides a scalar-reweighted fully-connected subgraph for

Table 1. Mean test set $\log_{10}(\text{MSE})$ and standard deviation on the Graph Property Prediction dataset. The lower the better.

Model	Diameter	SSSP	Eccentricity
GCN	0.7424 ± 0.0466	0.9499 ± 0.0001	0.8468 ± 0.0028
GAT	0.8221 ± 0.0752	0.6951 ± 0.1499	0.7909 ± 0.0222
GraphSAGE	0.8645 ± 0.0401	0.2863 ± 0.1843	0.7863 ± 0.0207
GIN	0.6131 ± 0.0990	-0.5408 ± 0.4193	0.9504 ± 0.0007
DGC	0.6028 ± 0.0050	-0.1483 ± 0.0231	0.8261 ± 0.0032
GRAND	0.6715 ± 0.0490	-0.0942 ± 0.3897	0.6602 ± 0.1393
A-DGN	0.2271 ± 0.0804	-1.8288 ± 0.0607	0.7177 ± 0.0345
ChebNet	-0.1517 ± 0.0343	-1.8519 ± 0.0539	-1.2151 ± 0.0852
Stable-ChebNet	-0.2477 ± 0.0526	-2.2111 ± 0.0160	-2.1043 ± 0.0766
S ² GNN	-0.1824 ± 0.0329	-2.103 ± 0.0386	-1.4622 ± 0.0815
DIFFormer	-0.2046 ± 0.0358	-1.9033 ± 0.0839	-1.4010 ± 0.0789
S ³ GNN (ours)	-0.3301 ± 0.0342	-2.6311 ± 0.0171	-2.4801 ± 0.0239

each connected component, we also compare S³GNN with graph transformer-based models, e.g., DIFFormer (Wu et al., 2023b), in which the feature dynamic is conducted via fully-connected graphs. Finally, we also compare our model with S²GNN as shown in Eq. (5).

Results and Computational Complexity The results are contained in Table 1. One can check that S³GNN consistently outperforms all baselines. Especially in the most challenging task, e.g., *Eccentricity*, S³GNN GNN yields an *order-of-magnitude* improvement compared to S²GNN, while consistently improving performance on *Diameter* and *SSSP*. In addition, unlike spectral methods like ChebNet and Stable-ChebNet, which require 4 to 6 layers and a 4th order polynomial to invoke the best results, our model achieves the best results with only 4 layers with cheaper computational cost. For example, assume \mathcal{G} is connected, the global mixing term in S³GNN reduces to a mean aggregation and can be computed in $\mathcal{O}(Nd)$, leading to a per-layer complexity $\mathcal{O}(|\mathcal{E}|d + Nd^2)$, whereas the complexity for both ChebNet and Stable-ChebNet is $\mathcal{O}(K|\mathcal{E}|d + Nd^2)$, roughly a factor- K higher propagation cost per layer. Finally, as aforementioned, the propagation of S²GNN requires eigen-decomposition, which incurs an additional computational cost (e.g., $\mathcal{O}(N^3)$ in the worst case) and makes it less scalable to large graphs.

α Dynamics Recall that one assumption in our theory is the mixing coefficient $\alpha_{\theta}^{(\ell)} > 0, \forall \ell$, and one expects $\alpha_{\theta}^{(\ell)}$ to become larger when ℓ is larger, where long-range communication between nodes is highly required. Interestingly,

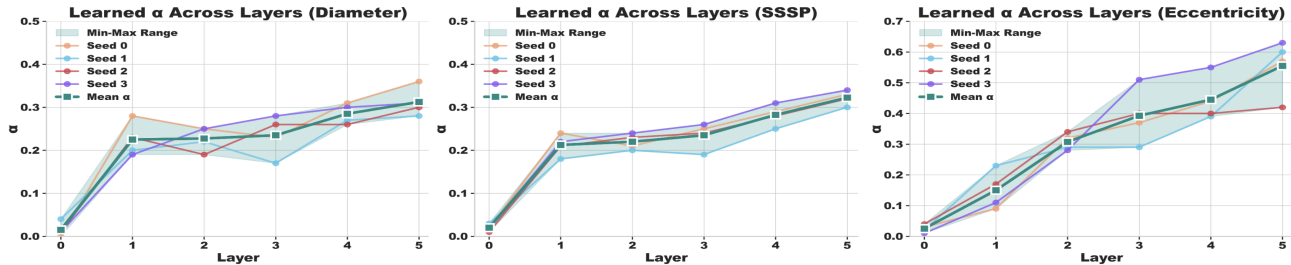
Figure 3. Changes of learned α values across the layers.

Table 2. Node classification accuracy on OGB datasets.

(a) Accuracy on ogbn-arxiv. (b) Accuracy on ogbn-proteins.

Model	ogbn-arxiv	Model	ogbn-proteins
GCN	71.74 \pm 0.29	MLP	72.04 \pm 0.48
ChebNet	73.27 \pm 0.23	GCN	72.51 \pm 0.35
ChebNetII	72.32 \pm 0.23	ChebNet	77.55 \pm 0.43
GraphSAGE	71.49 \pm 0.27	SGC	70.31 \pm 0.23
GAT	72.01 \pm 0.20	GCN-NSAMPLER	73.51 \pm 1.31
NodeFormer	59.90 \pm 0.42	GAT-NSAMPLER	74.63 \pm 1.24
GraphGPS	70.92 \pm 0.04	SIGN	71.24 \pm 0.46
GOAT	72.41 \pm 0.40	NodeFormer	77.45 \pm 1.15
EXPHORMER+GCN	72.44 \pm 0.28	SGFormer	79.53 \pm 0.38
SPEXPFORMER	70.82 \pm 0.24	SPEXPFORMER	80.65 \pm 0.07
DIFFORMER	72.21 \pm 0.33	DIFFORMER	77.69 \pm 0.25
Stable-ChebNet	75.42 \pm 0.28	Stable-ChebNet	79.89 \pm 0.18
S ² GCN	73.89 \pm 0.58	S ² GCN	80.58 \pm 0.72
S³GNN (ours)	76.38 \pm 0.32	S³GNN (ours)	81.90 \pm 0.12

we empirically observed that the non-negative assumption on α can be **automatically satisfied**, evidenced by Figure 1 where one learnable α leads to a positive theoretical lower bound and Figure 3 in which an increasing trend between α_θ and ℓ is consistently observed for all datasets. These findings indicate that the positivity and growth of $\alpha_\theta^{(\ell)}$ emerge naturally during training, rather than being enforced explicitly, thereby aligning the learned dynamics with the conditions required by our theoretical analysis.

Scalability over Large-Scale Datasets In addition to the graph-level tasks in graph property prediction datasets, we further evaluate the performance of S³GNN in node classification tasks via real-world large-scale datasets, e.g., *ogbn-arxiv* and *ogbn-proteins*. The results can be found in Table 2, where S³GNN shows outstanding results compared to multiple baselines. In particular, compared to those graph transformer-based methods, such as SGFormer (Wu et al., 2023c), Spexphormer (Shirzad et al., 2024), and DIFFormer (Wu et al., 2023b). This indicates that to account for the long-range interaction between distant nodes, one may simply need to add a scaler-adjusted low-rank global-mixing process as in S³GNN, rather than conducting a complex attention mechanism over any pair of nodes.

4.2. Long-Range Graph Benchmarks

Long-range graph benchmarks (LRGB) (Dwivedi et al., 2022) are designed to specifically test GNN performance on tasks where distant node information is important. We select

Table 3. Long-range benchmark results.

Model Type	Model	peptides-func (AP \uparrow)	peptides-struct (MAE \downarrow)
Transformer	SAN+LapPE	63.84 \pm 1.21	0.2683 \pm 0.0043
	TIGT	66.79 \pm 0.74	0.2485 \pm 0.0015
	Specformer	66.86 \pm 0.64	0.2550 \pm 0.0014
	Expformer	65.27 \pm 0.43	0.2481 \pm 0.0007
	G.MLPMixer	69.21 \pm 0.54	0.2475 \pm 0.0015
	Graph ViT	69.42 \pm 0.75	0.2449 \pm 0.0016
	GRIT	69.88 \pm 0.82	0.2460 \pm 0.0012
Rewiring	LASER	64.40 \pm 0.10	0.3043 \pm 0.0019
	DRew-GCN	69.96 \pm 0.76	0.2781 \pm 0.0028
	+PE	71.50 \pm 0.44	0.2536 \pm 0.0015
State Space	Graph Mamba	67.39 \pm 0.87	0.2478 \pm 0.0016
	GMN	70.71 \pm 0.83	0.2473 \pm 0.0025
	MP-SSM	69.93 \pm 0.52	0.2458 \pm 0.0017
VN	GCN+VN	65.40 \pm 0.66	0.2509 \pm 0.0030
	GatedGCN+VN \dagger	68.80 \pm 0.47	0.2460 \pm 0.0021
	GatedGCN+VN \ddagger	68.10 \pm 0.33	0.2498 \pm 0.0042
	GCN+FN	67.80 \pm 0.54	0.2456 \pm 0.0019
	GatedGCN+FN	69.50 \pm 0.47	0.2470 \pm 0.0039
GNN	A-DGN	59.75 \pm 0.44	0.2874 \pm 0.0021
	ChebNet	69.61 \pm 0.33	0.2627 \pm 0.0033
	GCN	68.60 \pm 0.50	0.2460 \pm 0.0007
	GRAND	57.89 \pm 0.62	0.3418 \pm 0.0015
	GraphCON	60.22 \pm 0.68	0.2778 \pm 0.0018
	SWAN	67.51 \pm 0.39	0.2485 \pm 0.0009
	S ² GNN	72.75 \pm 0.66	0.2487 \pm 0.0019
	+PE	73.11 \pm 0.66	0.2447 \pm 0.0032
	Stable-ChebNet	70.32 \pm 0.26	0.2542 \pm 0.0030
	S³GNN	73.20 \pm 0.14	0.2429 \pm 0.0014

peptides-func and *peptides-struct*, with the former as a graph classification evaluated by average precision (AP), and the latter as graph regression evaluated by mean absolute error (MAE). The results are presented in Table 3, where S³GNN shows leading performance compared to several baseline architectures. Interestingly, we did not observe strong performance for those spatial rewiring methods, such as LASER (Barbero et al., 2024) and DRew (Gutteridge et al., 2023). Instead, GNNs that propagate feature information in a global manner, such as S²GNN and Stable-ChebNet, consistently outperform other baselines. However, compared to Stable-ChebNet, the learning accuracy gain of S²GNN may be due to the additional spatial part and the positional encoding (PE), which requires high-cost eigendecomposition of every input graph. On the other hand, our S³GNN outperforms Stable-ChebNet without conducting eigendecomposition and PE. This suggests that explicitly enhancing global information exchange is a more effective strategy for these long-range graph tasks, and S³GNN achieves this advantage with a *lightweight design and low computational overhead*.

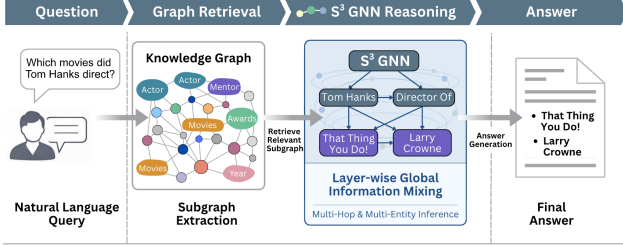


Figure 4. Illustration of multi-hop/entity KGQA with S³GNN.

Table 4. Performance on multi-hop and multi-entity questions.

Method	WebQSP (F1)		CWQ (F1)		MetaQA-3 (H@1)
	multi-hop	multi-entity	multi-hop	multi-entity	multi-hop
LLM (No RAG)	48.4	61.5	33.7	32.3	29.7
Reasoning GNN	58.8	70.4	57.7	54.2	98.6
Reasoning S ³ GNN	69.6	73.0	68.8	61.1	98.8
Improvement	+10.8%	+2.6%	+11.1%	+6.9%	+0.2%
RoG	63.3	65.1	59.3	58.3	84.8
SubgraphRAG	65.8	54.9	55.8	52.3	—
Reasoning GNN-RAG	69.8	82.3	68.2	64.8	98.6
Reasoning S ³ GNN-RAG	70.3	85.5	68.8	64.9	98.9
Improvement	+0.5%	+3.2%	+0.6%	+0.1%	+0.3%

4.3. Multi-Hop/Entity KGQA

Knowledge Graph Question Answering (KGQA) aims to answer natural language questions by reasoning over structured knowledge graphs composed of entities and relations (Pan et al., 2024). While recent LLM have shown strong performance on simple factual queries, they often struggle when questions require reasoning over multiple hops or involve multiple query entities, due to the combinatorial expansion of the graph context and the difficulty of reliably identifying relevant relational paths. As a result, multi-hop and multi-entity questions are regarded as among the most challenging settings in KGQA (Mavromatis & Karypis, 2022).

Following recent work on deploying GNNs for effective graph retrieval (Mavromatis & Karypis, 2024), we study KGQA under a retrieval-augmented (RAG) setting, where the model (e.g., Reasoning GNN (Mavromatis & Karypis, 2022)) first retrieves a compact subgraph relevant to the question and then performs reasoning on the retrieved evidence. In this experiment, GNN-based retrieval is particularly focused on multi-hop and multi-entity queries (hops/entities ≥ 2), and we replace the original message-passing dynamics of the reasoning GNN with S³GNN, while leaving the remaining RAG pipeline unchanged. We evaluate on the multi-hop and multi-entity subsets of *WebQSP* and *CWQ*, and the multi-hop split of *MetaQA-3*, and report the corresponding F1/H@1 metrics. Figure 4 illustrates the multi-hop/entity KGQA process and the role of S³GNN.

Results From the results in Table 4, S³GNN consistently improves performance in both the presence and absence of RAG. We further observe that, in some cases, the gains

Table 5. Overall 1 (left) and square root (right) 2-Wasserstein distances on brain signals, lower is the better.

Method	Brain signals	
TSB-BM-GCN	7.51 \pm 0.08	5.51 \pm 0.06
TSB-VE-GCN	7.59 \pm 0.05	5.55 \pm 0.04
TSB-VP-GCN	7.67 \pm 0.11	5.64 \pm 0.09
TSB-BM-S ³ GNN	7.25 \pm 0.05	5.29 \pm 0.18
TSB-VE-S ³ GNN	7.22 \pm 0.03	5.24 \pm 0.10
TSB-VP-S ³ GNN	7.29 \pm 0.05	5.30 \pm 0.05

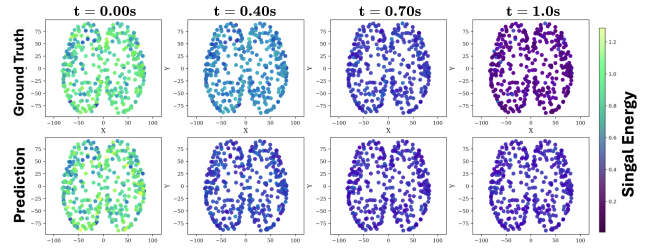


Figure 5. Interpolation results of TSB-VE-S³GNN. Our model successfully produces the intermediate energy distributions between the initial and ending brain signals.

obtained by adopting S³GNN are sufficient to surpass the performance of a reasoning GNN equipped with RAG (e.g., 68.8 V.S 68.2 in *CWQ* multi-hop F1 score). This suggests that a more suitable GNN dynamics in the reasoning module may partially substitute explicit retrieval mechanisms and lead to stronger QA performance.

4.4. Topological Interpolation

In this experiment, we show S³GNN can be a strong backbone model for topological interpolation. Specifically, we consider the topological Schrodinger bridge matching (TSBM) model proposed in (Yang, 2025), in which we are interested in predicting the intermediate energy distributions between high and low energy brain signals (Van Essen et al., 2013). The training of TSBM is conducted by using an alternating scheme and both forward and backward processes governed by the graph stochastic heat diffusion equation $dX_t = -cLX_t dt + g_t dW_t$. Fixing $X_T \sim p_T$ (prior) and $X_0 \sim p_0$ (posterior), TSBM seeks to fit two GNNs $\phi_{\#}$ and ϕ_{\square} for forward and backward SDEs for brain signals,

$$dX_t = (-cLX_t + g_t^2 \nabla_x \log \phi_{\#}(t)(X_t))dt + g_t dW_t. \quad (12)$$

Here, ∇_x is the gradient of the feature vectors and the backward SDE can be obtained by replacing $\phi_{\#}$ with ϕ_{\square} . Our motivation for deploying S³GNN to this task is grounded in neuroscience evidence that transitions of brain signals across different energy states are governed by large-scale functional connectivity and long-range interactions among distant regions, thereby necessitating explicit global infor-

Table 6. Results (RMSE) on Cylinder Flow, the lower is better.

Metric	MGN	S ³ MGN
Min Test Loss	0.173	0.102 (41%↓)
Min Train Loss	0.138	0.067 (51%↓)
Min Velocity RMSE	0.000589	0.000333 (43%↓)

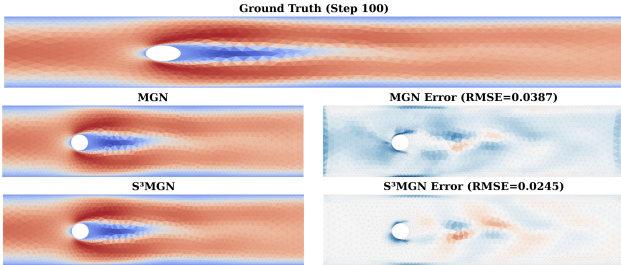


Figure 6. Cylinder flow visualization (Step 100). Top: ground-truth velocity field. Middle/Bottom: predictions from MGN and S³MGN with corresponding error maps.

mation exchange during propagation (Greicius et al., 2003; Bassett & Bullmore, 2006). Accordingly, one would expect GNNs that propagate node features in a global manner to be a better model in terms of approximating the score functions (e.g., $\nabla_x \log \phi_{\#}(t)(X_t)$) in Eq. (12). The results are presented in Table 5 and Figure 5. Rather than observing that S³GNN assisted TSB models consistently outperform their GCN counterparts, one can also find that the differences between three types of TSB models, i.e., standard Brownian motion (BM), variance explode (VE) and variance perserving (VP), are relatively smaller than the performance gap induced by replacing the GCN backbone with S³GNN. We conjecture that the improvements are related to the explicit global information exchange in S³GNN, which is consistent with the long-range interactions in brain signals. This points to a promising direction of integrating task-suitable GNN backbones with (topological) generative modeling frameworks for different data domains.

4.5. Mesh-based Fluid Dynamics Prediction

We evaluate S³GNN as a backbone for mesh-based fluid prediction on the cylinder-flow benchmark (Pfaff et al., 2020). At each discrete time step, the spatially discretized flow field is represented as a mesh graph with fixed topology, where node features encode the instantaneous physical states. Given the state at time t , the model predicts per-node acceleration (or velocity increment) \hat{a}_t , and we obtain the next-step velocity by explicit integration: $\hat{v}_{t+1} = v_t + \Delta t \cdot \hat{a}_t$. Our S³MeshGraphNet (S³MGN) follows the standard MeshGraphNet (MGN) encoder–processor–decoder pipeline, but replaces the processor blocks with S³GNN layers. This design is motivated by the long-range couplings in cylinder wakes, where effective coordination between distant mesh regions is beneficial for stable rollout prediction.

We evaluate both one-step prediction and multi-step rollouts

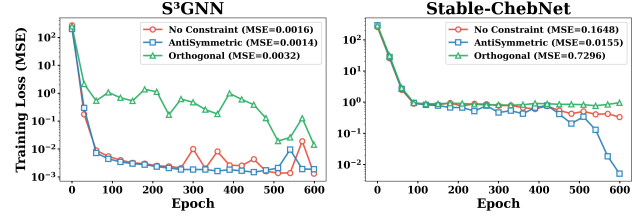


Figure 7. Ablation study in Barbell graph with different constraints.

by repeatedly applying the learned dynamics. The quantitative comparison is reported in Table 6, where S³MGN consistently improves over the MGN baseline across training/test objectives and velocity RMSE. In addition, Figure 6 visualizes a long-horizon rollout (Step 100), where S³MGN yields a lower RMSE and noticeably reduced errors in the wake region compared to MGN.

4.6. Ablation and Future Studies

Finally, we conduct ablation studies on constraints imposed on \mathbf{W} , including a free \mathbf{W} , an antisymmetric $\widehat{\mathbf{W}}$ (as in S³GNN), and an orthogonal \mathbf{W} , where the latter is expected to further tighten the bound of $\|\partial \mathbf{h}_i(\ell)/\partial \mathbf{x}_s\|$ as discussed in Section 3.3. As shown in Figure 7, both Stable-ChebNet and S³GNN achieve the best performance with the antisymmetric constraint. Notably, the gap between free \mathbf{W} and antisymmetric $\widehat{\mathbf{W}}$ is much smaller in S³GNN than in Stable-ChebNet, suggesting that the benefit of constraining \mathbf{W} depends on the propagation mechanism (e.g., spatial vs. spectral) and the task. Moreover, while orthogonality can more strongly tighten the bound of $\|\partial \mathbf{h}_i(\ell)/\partial \mathbf{x}_s\|$, it also substantially shrinks the feasible space of \mathbf{W} , which may hinder task-specific adaptation and lead to a more unstable optimization behavior. In contrast, antisymmetry appears to regulate the variation of the Jacobian in a more parameter-efficient way, providing a better stability–expressivity trade-off in this setting. These observations motivate future work on how to choose the appropriate degree of constraint for different propagation schemes and long-range learning tasks.

5. Conclusion

In this work, we identified a gap between recent theoretical OSQ-mitigation guarantees and their practical attainability in graph neural networks. To address this issue, we proposed S³GNN, a lightweight global–local propagation framework that achieves effective long-range information mixing without relying on restrictive spectral assumptions or expensive eigendecomposition. We further showed that standard stability constraints on feature transformations remain effective under the proposed dynamics, continuing to stabilize the Jacobian energy across depth. Extensive experiments across diverse domains demonstrate that S³GNN delivers strong long-range performance with substantially reduced computational and parameter costs.

References

- Alon, U. and Yahav, E. On the bottleneck of graph neural networks and its practical implications. In *International Conference on Learning Representations*, 2020.
- Arnaiz-Rodriguez, A. and Errica, F. Oversmoothing,” oversquashing”, heterophily, long-range, and more: Demystifying common beliefs in graph machine learning. *arXiv:2505.15547*, 2025.
- Bamberger, J., Barbero, F., Dong, X., and Bronstein, M. M. Bundle neural network for message diffusion on graphs. In *International Conference on Learning Representations*, 2025.
- Banerjee, P. K., Karhadkar, K., Wang, Y. G., Alon, U., and Montúfar, G. Oversquashing in GNNs through the lens of information contraction and graph expansion. In *The 58th Annual Allerton Conference on Communication, Control, and Computing*, pp. 1–8. IEEE, 2022.
- Barbero, F., Velingker, A., Saberi, A., Bronstein, M., and Di Giovanni, F. Locality-aware graph-rewiring in GNNs. *International Conference on Learning Representations*, 2024.
- Bassett, D. S. and Bullmore, E. Small-world brain networks. *The neuroscientist*, 12(6):512–523, 2006.
- Behrouz, A. and Hashemi, F. Graph mamba: Towards learning on graphs with state space models. In *Proceedings of the 30th ACM SIGKDD conference on knowledge discovery and data mining*, pp. 119–130, 2024.
- Black, M., Wan, Z., Nayyeri, A., and Wang, Y. Understanding oversquashing in GNNs through the lens of effective resistance. In *International Conference on Machine Learning*, pp. 2528–2547. PMLR, 2023.
- Bo, D., Shi, C., Wang, L., and Liao, R. Specformer: Spectral graph neural networks meet transformers. *arXiv preprint arXiv:2303.01028*, 2023.
- Chamberlain, B., Rowbottom, J., Eynard, D., Di Giovanni, F., Dong, X., and Bronstein, M. Beltrami flow and neural diffusion on graphs. In *Advances in Neural Information Processing Systems*, volume 34, pp. 1594–1609. Curran Associates, Inc., 2021a. URL https://proceedings.neurips.cc/paper_files/paper/2021/file/0cbed40c0d920b94126eaf5e707belf5-Paper.pdf.
- Chamberlain, B., Rowbottom, J., Gorinova, M. I., Bronstein, M., Webb, S., and Rossi, E. Grand: Graph neural diffusion. In *International Conference on Machine Learning*, pp. 1407–1418. PMLR, 2021b.
- Choi, J., Park, S., Wi, H., Cho, S., and Park, N. PANDA: expanded width-aware message passing beyond rewiring. In *International Conference on Machine Learning*, 2024a.
- Choi, Y. Y., Park, S. W., Lee, M., and Woo, Y. Topology-informed graph transformer. *arXiv preprint arXiv:2402.02005*, 2024b.
- Corso, G., Cavalleri, L., Beaini, D., Liò, P., and Veličković, P. Principal neighbourhood aggregation for graph nets. *Advances in neural information processing systems*, 33: 13260–13271, 2020.
- Deac, A., Lackenby, M., and Veličković, P. Expander graph propagation. In *Learning on Graphs Conference*, pp. 38–1. PMLR, 2022.
- Defferrard, M., Bresson, X., and Vandergheynst, P. Convolutional neural networks on graphs with fast localized spectral filtering. *Advances in Neural Information Processing Systems*, 29, 2016.
- Di Giovanni, F., Rusch, T. K., Bronstein, M. M., Deac, A., Lackenby, M., Mishra, S., and Veličković, P. How does over-squashing affect the power of gnn’s? *Transactions on Machine Learning Research*, 2024.
- Dwivedi, V. P., Rampášek, L., Galkin, M., Parviz, A., Wolf, G., Luu, A. T., and Beaini, D. Long range graph benchmark. In *Advances in Neural Information Processing Systems*, volume 35, pp. 22326–22340, 2022.
- Fesser, L., Iváñez, S. S. d. H., Devriendt, K., Weber, M., and Lambiotte, R. Augmentations of Forman’s Ricci curvature and their applications in community detection. *arXiv:2306.06474*, 2023.
- Geisler, S. M., Kosmala, A., Herbst, D., and Günnemann, S. Spatio-spectral graph neural networks. *Advances in Neural Information Processing Systems*, 37:49022–49080, 2024.
- Gilmer, J., Schoenholz, S. S., Riley, P. F., Vinyals, O., and Dahl, G. E. Neural message passing for quantum chemistry. In *International Conference on Machine Learning*, pp. 1263–1272. PMLR, 2017.
- Giraldo, J. H., Malliaros, F. D., and Bouwmans, T. Understanding the relationship between oversmoothing and over-squashing in graph neural networks. *arXiv:2212.02374*, 2022.
- Gravina, A., Bacciu, D., and Gallicchio, C. Anti-symmetric dgn: a stable architecture for deep graph networks. *arXiv preprint arXiv:2210.09789*, 2022.
- Greicius, M. D., Krasnow, B., Reiss, A. L., and Menon, V. Functional connectivity in the resting brain: a network

- analysis of the default mode hypothesis. *Proceedings of the national academy of sciences*, 100(1):253–258, 2003.
- Gutteridge, B., Dong, X., Bronstein, M. M., and Di Giovanni, F. Drew: Dynamically rewired message passing with delay. In *International Conference on Machine Learning*, pp. 12252–12267. PMLR, 2023.
- Hamilton, W., Ying, Z., and Leskovec, J. Inductive representation learning on large graphs. *Advances in Neural Information Processing Systems*, 30, 2017.
- Hariri, A., Arroyo, Á., Gravina, A., Eliasof, M., Schönlieb, C.-B., Bacciu, D., Azzadenesheli, K., Dong, X., and Vanderghenst, P. Return of chebnet: Understanding and improving an overlooked gnn on long range tasks. *arXiv preprint arXiv:2506.07624*, 2025.
- He, M., Wei, Z., and Wen, J.-R. Convolutional neural networks on graphs with chebyshev approximation, revisited. *Advances in neural information processing systems*, 35: 7264–7276, 2022.
- He, X., Hooi, B., Laurent, T., Perold, A., LeCun, Y., and Bresson, X. A generalization of ViT/MLP-Mixer to graphs. In *International Conference on Machine Learning*, pp. 12724–12745. PMLR, 2023.
- Ji, S., Pan, S., Cambria, E., Marttinen, P., and Philip, S. Y. A survey on knowledge graphs: Representation, acquisition, and applications. *IEEE transactions on neural networks and learning systems*, 33(2):494–514, 2021.
- Karhadkar, K., Banerjee, P. K., and Montúfar, G. Fcsr: First-order spectral rewiring for addressing oversquashing in gnns. In *International Conference on Learning Representations*, 2023.
- Kipf, T. N. and Welling, M. Semi-supervised classification with graph convolutional networks. *arXiv:1609.02907*, 2016.
- Kipf, T. N. and Welling, M. Semi-supervised classification with graph convolutional networks. In *International Conference on Learning Representations*, 2017.
- Kong, K., Chen, J., Kirchenbauer, J., Ni, R., Bruss, C. B., and Goldstein, T. Goat: A global transformer on large-scale graphs. In *International Conference on Machine Learning*, pp. 17375–17390. PMLR, 2023.
- Kreuzer, D., Beaini, D., Hamilton, W., Létourneau, V., and Tossou, P. Rethinking graph transformers with spectral attention. *Advances in Neural Information Processing Systems*, 34:21618–21629, 2021.
- Ma, L., Lin, C., Lim, D., Romero-Soriano, A., Dokania, P. K., Coates, M., Torr, P., and Lim, S.-N. Graph inductive biases in transformers without message passing. In *International Conference on Machine Learning*, pp. 23321–23337. PMLR, 2023.
- Mavromatis, C. and Karypis, G. Rearev: Adaptive reasoning for question answering over knowledge graphs. *arXiv preprint arXiv:2210.13650*, 2022.
- Mavromatis, C. and Karypis, G. Gnn-rag: Graph neural retrieval for large language model reasoning. *arXiv preprint arXiv:2405.20139*, 2024.
- Mishra, S. mhc-gnn: Manifold-constrained hyperconnections for graph neural networks. *arXiv preprint arXiv:2601.02451*, 2026.
- Nguyen, K., Hieu, N. M., Nguyen, V. D., Ho, N., Osher, S., and Nguyen, T. M. Revisiting over-smoothing and over-squashing using Ollivier-Ricci curvature. In *International Conference on Machine Learning*, pp. 25956–25979. PMLR, 2023.
- Pan, S., Luo, L., Wang, Y., Chen, C., Wang, J., and Wu, X. Unifying large language models and knowledge graphs: A roadmap. *IEEE Transactions on Knowledge and Data Engineering*, 36(7):3580–3599, 2024.
- Pei, H., Li, Y., Deng, H., Hai, J., Wang, P., Ma, J., Tao, J., Xiong, Y., and Guan, X. Multi-track message passing: Tackling oversmoothing and oversquashing in graph learning via preventing heterophily mixing. In *International Conference on Machine Learning*, 2024.
- Pfaff, T., Fortunato, M., Sanchez-Gonzalez, A., and Battaglia, P. Learning mesh-based simulation with graph networks. In *International conference on learning representations*, 2020.
- Rampásek, L., Galkin, M., Dwivedi, V. P., Luu, A. T., Wolf, G., and Beaini, D. Recipe for a general, powerful, scalable graph transformer. In *Advances in Neural Information Processing Systems*, volume 35, pp. 14501–14515, 2022.
- Rusch, T. K., Bronstein, M. M., and Mishra, S. A survey on oversmoothing in graph neural networks. *arXiv:2303.10993*, 2023.
- Sato, R. A survey on the expressive power of graph neural networks. *arXiv:2003.04078*, 2020.
- Shi, D., Gao, J., Hong, X., Boris Choy, S., and Wang, Z. Coupling matrix manifolds assisted optimization for optimal transport problems. *Machine Learning*, 110(3): 533–558, 2021.
- Shi, D., Han, A., Lin, L., Guo, Y., and Gao, J. Exposition on over-squashing problem on gnns: Current methods, benchmarks and challenges. *arXiv preprint arXiv:2311.07073*, 2023.

- Shirzad, H., Velingker, A., Venkatachalam, B., Sutherland, D. J., and Sinop, A. K. Exphormer: Sparse transformers for graphs. In *International Conference on Machine Learning*, pp. 31613–31632. PMLR, 2023.
- Shirzad, H., Lin, H., Venkatachalam, B., Velingker, A., Woodruff, D. P., and Sutherland, D. J. Even sparser graph transformers. *Advances in Neural Information Processing Systems*, 37:71277–71305, 2024.
- Thorpe, M., Nguyen, T. M., Xia, H., Strohmer, T., Bertozzi, A., Osher, S., and Wang, B. GRAND++: Graph neural diffusion with a source term. In *International Conference on Learning Representations*, 2022. URL <https://openreview.net/forum?id=EMxu-dzvJk>.
- Topping, J., Di Giovanni, F., Chamberlain, B. P., Dong, X., and Bronstein, M. M. Understanding over-squashing and bottlenecks on graphs via curvature. In *International Conference on Learning Representations*, 2021.
- Toth, C., Lee, D., Hacker, C., and Oberhauser, H. Capturing graphs with hypo-elliptic diffusions. *Advances in Neural Information Processing Systems*, 35:38803–38817, 2022.
- Van Essen, D. C., Smith, S. M., Barch, D. M., Behrens, T. E., Yacoub, E., Ugurbil, K., Consortium, W.-M. H., et al. The wu-minn human connectome project: an overview. *Neuroimage*, 80:62–79, 2013.
- Veličković, P., Cucurull, G., Casanova, A., Romero, A., Liò, P., and Bengio, Y. Graph attention networks. In *International Conference on Learning Representations*, 2018.
- Wang, C., Tsepa, O., Ma, J., and Wang, B. Graph-mamba: Towards long-range graph sequence modeling with selective state spaces. *arXiv preprint arXiv:2402.00789*, 2024.
- Wu, Q., Zhao, W., Li, Z., Wipf, D. P., and Yan, J. Nodeformer: A scalable graph structure learning transformer for node classification. In *Advances in Neural Information Processing Systems*, volume 35, pp. 27387–27401, 2022.
- Wu, Q., Yang, C., Zhao, W., He, Y., Wipf, D., and Yan, J. Difformer: Scalable (graph) transformers induced by energy constrained diffusion. In *International Conference on Learning Representations*, 2023a.
- Wu, Q., Yang, C., Zhao, W., He, Y., Wipf, D., and Yan, J. Difformer: Scalable (graph) transformers induced by energy constrained diffusion. *arXiv:2301.09474*, 2023b.
- Wu, Q., Zhao, W., Yang, C., Zhang, H., Nie, F., Jiang, H., Bian, Y., and Yan, J. Sgformer: Simplifying and empowering transformers for large-graph representations. *Advances in Neural Information Processing Systems*, 36: 64753–64773, 2023c.
- Wu, Z., Pan, S., Chen, F., Long, G., Zhang, C., and Philip, S. Y. A comprehensive survey on graph neural networks. *IEEE transactions on Neural Networks and Learning Systems*, 32(1):4–24, 2020.
- Xie, Z., Wei, Y., Cao, H., Zhao, C., Deng, C., Li, J., Dai, D., Gao, H., Chang, J., Zhao, L., et al. mhc: Manifold-constrained hyper-connections. *arXiv preprint arXiv:2512.24880*, 2025.
- Xu, K., Hu, W., Leskovec, J., and Jegelka, S. How powerful are graph neural networks? In *International Conference on Learning Representations*, 2019. URL <https://openreview.net/forum?id=ryGs6iA5Km>.
- Yang, M. Topological schrödinger bridge matching. In *The Thirteenth International Conference on Learning Representations*, 2025. URL <https://openreview.net/forum?id=WzCEiBILHu>.
- Ying, C., Cai, T., Luo, S., Zheng, S., Ke, G., He, D., Shen, Y., and Liu, T.-Y. Do transformers really perform badly for graph representation? *Advances in Neural Information Processing Systems*, 34:28877–28888, 2021.

A. Related Works

OSQ Mitigation Methods Oversquashing arises when information from exponentially many distant nodes is compressed into fixed-dimensional node representations, and has been recognized as a fundamental limitation of message-passing GNNs (Topping et al., 2021; Shi et al., 2023; Alon & Yahav, 2020). Existing mitigation methods can be broadly categorized into three lines. (1) *Spatial rewiring* directly modifies the graph connectivity (i.e., the adjacency) by adding shortcut edges, typically connecting nodes within an r -hop neighborhood (Topping et al., 2021; Giraldo et al., 2022). (2) *Spectral rewiring* aims to add edges so as to improve global expansion-related properties of the graph, such as the spectral gap (Karhadkar et al., 2023), total effective resistance (Black et al., 2023), and commute time (Di Giovanni et al., 2024). (3) *Implicit rewiring* constructs better effective connectivity (e.g., denser, reweighted, or fully connected graphs) as a by-product of architectures originally motivated by other considerations, including graph transformers and their variants (Ying et al., 2021; Wu et al., 2022; 2023a), diffusion-based MPNNs (Thorpe et al., 2022; Chamberlain et al., 2021a; Toth et al., 2022), and multi-track feature propagation methods (Pei et al., 2024; Choi et al., 2024a). We refer the recent survey and positional paper on OSQ problem for more details (Shi et al., 2023; Arnaiz-Rodriguez & Errica, 2025).

B. Theoretical Proofs

Proof of Proposition 1. Fix a connected component \mathcal{C}_r with $|\mathcal{C}_r| = n_r$ and take any $i, s \in \mathcal{C}_r$. For convenience, write the layer operator in Eq. (9) as

$$\mathbf{H}(\ell + 1) = \mathbf{M}(\ell) \mathbf{H}(\ell) \mathbf{W}(\ell), \quad \mathbf{M}(\ell) := \widehat{\mathbf{A}} + \mathbf{P}_\theta(\ell).$$

By construction of the 0-eigenspace basis $\{\mathbf{v}^{(r)}\}$ on connected components, $\mathbf{P}_\theta(\ell)$ is block-constant on \mathcal{C}_r , hence for all $u, v \in \mathcal{C}_r$,

$$(\mathbf{P}_\theta(\ell))_{uv} = \frac{\alpha_{\theta,r}^{(\ell)}}{n_r}, \quad (\mathbf{P}_\theta(\ell))_{uv} = 0 \text{ if } u \notin \mathcal{C}_r \text{ or } v \notin \mathcal{C}_r. \quad (13)$$

In particular, $(\mathbf{M}(\ell))_{uv} \geq (\mathbf{P}_\theta(\ell))_{uv} \geq 0$.

Let $\mathbf{h}_i(\ell) \in \mathbb{R}^d$ denote the feature of node i at layer ℓ (a row vector), and define $\mathbf{J}_{is}(\ell) := \frac{\partial \mathbf{h}_i(\ell)}{\partial \mathbf{x}_s} \in \mathbb{R}^{d \times d}$. Since the forward map is linear in $\mathbf{H}(\ell)$ at each layer, repeated application of the chain rule gives

$$\mathbf{J}_{is}(\ell) = \left(\mathbf{M}(\ell - 1) \mathbf{M}(\ell - 2) \cdots \mathbf{M}(0) \right)_{is} \cdot \left(\mathbf{W}(0) \mathbf{W}(1) \cdots \mathbf{W}(\ell - 1) \right), \quad (14)$$

with $\mathbf{J}_{is}(0) = \mathbf{I}_d$ when $i = s$ and $\mathbf{0}$ otherwise.

We now lower bound the scalar coefficient in (14). Because all entries of $\mathbf{M}(p)$ are nonnegative, for any $i, s \in \mathcal{C}_r$,

$$\left(\mathbf{M}(\ell - 1) \cdots \mathbf{M}(0) \right)_{is} \geq \left(\mathbf{P}_\theta(\ell - 1) \cdots \mathbf{P}_\theta(0) \right)_{is}.$$

Moreover, using (13), for every p and every $u, v \in \mathcal{C}_r$, $(\mathbf{P}_\theta(p))_{uv} = \alpha_{\theta,r}^{(p)}/n_r$, hence

$$\left(\mathbf{P}_\theta(\ell - 1) \cdots \mathbf{P}_\theta(0) \right)_{is} = \prod_{p=0}^{\ell-1} \frac{\alpha_{\theta,r}^{(p)}}{n_r}.$$

Combining the last two displays yields

$$\left(\mathbf{M}(\ell - 1) \cdots \mathbf{M}(0) \right)_{is} \geq \prod_{p=0}^{\ell-1} \frac{\alpha_{\theta,r}^{(p)}}{n_r}. \quad (15)$$

Finally, let

$$\mathbf{W}_{\text{tot}}(\ell) := \mathbf{W}(0) \mathbf{W}(1) \cdots \mathbf{W}(\ell - 1).$$

By the assumption $\sigma_{\min}(\mathbf{W}(p)) > 0$ for all p , we have $\sigma_{\min}(\mathbf{W}_{\text{tot}}(\ell)) \geq \prod_{p=0}^{\ell-1} \sigma_{\min}(\mathbf{W}(p))$.

Then, by (14) and (15),

$$\begin{aligned} \left\| \frac{\partial \mathbf{h}_i(\ell)}{\partial \mathbf{x}_s} \right\| &= \|\mathbf{J}_{is}(\ell)\| \\ &= \left(\mathbf{M}(\ell-1) \cdots \mathbf{M}(0) \right)_{is} \cdot \|\mathbf{W}_{\text{tot}}(\ell)\| \geq \left(\prod_{p=0}^{\ell-1} \frac{\alpha_{\theta,r}^{(p)}}{n_r} \right) \left(\prod_{p=0}^{\ell-1} \sigma_{\min}(\mathbf{W}(p)) \right). \end{aligned}$$

Multiplying the right-hand side by ε^ℓ (consistent with the ε -scaling in Eq. (9)) gives exactly (10). The lower bound depends only on n_r and the per-layer parameters $\alpha_{\theta,r}^{(p)}$ and $\mathbf{W}(p)$, and is independent of the graph distance between i and s within \mathcal{C}_r . Furthermore, the lower bound for the model using different \mathbf{W} for spatial and spectral parts can be obtained by following the same strategy, with additional consideration on the interactive terms between weight matrices; we omit it here. \square

Proof of Proposition 2. The proof follows the similar strategy in (Hariri et al., 2025). The core is the outer product between one antisymmetric matrix and a symmetric matrix is still antisymmetric, i.e., $\mathbf{P}_\theta \otimes \widehat{\mathbf{W}}$ and $\mathbf{A} \otimes \widehat{\mathbf{W}}$.

Let $\mathbf{h}(\ell) = \text{vec}(\mathbf{H}(\ell)) \in \mathbb{R}^{Nd}$. Using the standard identity

$$\text{vec}(\mathbf{S} \mathbf{H} \mathbf{W}) = (\mathbf{W}^\top \otimes \mathbf{S}) \text{vec}(\mathbf{H}),$$

the dynamics in Eq. (11) implies

$$\begin{aligned} \mathbf{h}(\ell+1) &= \mathbf{h}(\ell) + \varepsilon \left(\text{vec}(\mathbf{P}_\theta(\ell) \mathbf{H}(\ell) \widehat{\mathbf{W}}(\ell)) + \text{vec}(\widehat{\mathbf{A}} \mathbf{H}(\ell) \widehat{\mathbf{W}}(\ell)) \right) \\ &= \mathbf{h}(\ell) + \varepsilon \left(\widehat{\mathbf{W}}(\ell)^\top \otimes \mathbf{P}_\theta(\ell) + \widehat{\mathbf{W}}(\ell)^\top \otimes \widehat{\mathbf{A}} \right) \mathbf{h}(\ell) \\ &= \left(\mathbf{I}_{Nd} + \varepsilon \mathbf{A}_{\text{tot}}(\ell) \right) \mathbf{h}(\ell), \end{aligned} \tag{16}$$

where

$$\mathbf{A}_{\text{tot}}(\ell) := \widehat{\mathbf{W}}(\ell)^\top \otimes (\mathbf{P}_\theta(\ell) + \widehat{\mathbf{A}}) \in \mathbb{R}^{Nd \times Nd}.$$

Therefore the layer Jacobian with respect to $\mathbf{h}(\ell)$ is

$$\mathbf{J}(\ell) = \frac{\partial \mathbf{h}(\ell+1)}{\partial \mathbf{h}(\ell)} = \mathbf{I}_{Nd} + \varepsilon \mathbf{A}_{\text{tot}}(\ell).$$

We now show that $\mathbf{A}_{\text{tot}}(\ell)$ is antisymmetric. By construction, $\widehat{\mathbf{W}}(\ell)$ is antisymmetric, i.e., $\widehat{\mathbf{W}}(\ell)^\top = -\widehat{\mathbf{W}}(\ell)$. Moreover, both $\mathbf{P}_\theta(\ell)$ and $\widehat{\mathbf{A}}$ are symmetric. Hence $\mathbf{P}_\theta(\ell) + \widehat{\mathbf{A}}$ is symmetric, and using $(\mathbf{X} \otimes \mathbf{Y})^\top = \mathbf{X}^\top \otimes \mathbf{Y}^\top$ gives

$$\mathbf{A}_{\text{tot}}(\ell)^\top = \widehat{\mathbf{W}}(\ell) \otimes (\mathbf{P}_\theta(\ell) + \widehat{\mathbf{A}}) = -\widehat{\mathbf{W}}(\ell)^\top \otimes (\mathbf{P}_\theta(\ell) + \widehat{\mathbf{A}}) = -\mathbf{A}_{\text{tot}}(\ell).$$

Thus $\mathbf{A}_{\text{tot}}(\ell)$ is antisymmetric.

Finally,

$$\begin{aligned} \mathbf{J}(\ell)^\top \mathbf{J}(\ell) &= (\mathbf{I}_{Nd} + \varepsilon \mathbf{A}_{\text{tot}}(\ell)^\top) (\mathbf{I}_{Nd} + \varepsilon \mathbf{A}_{\text{tot}}(\ell)) \\ &= \mathbf{I}_{Nd} + \varepsilon (\mathbf{A}_{\text{tot}}(\ell) + \mathbf{A}_{\text{tot}}(\ell)^\top) + \varepsilon^2 \mathbf{A}_{\text{tot}}(\ell)^\top \mathbf{A}_{\text{tot}}(\ell) \\ &= \mathbf{I}_{Nd} + \varepsilon^2 \mathbf{A}_{\text{tot}}(\ell)^\top \mathbf{A}_{\text{tot}}(\ell), \end{aligned} \tag{17}$$

where the linear term vanishes since $\mathbf{A}_{\text{tot}}(\ell)^\top = -\mathbf{A}_{\text{tot}}(\ell)$. Because $\mathbf{A}_{\text{tot}}(\ell)^\top \mathbf{A}_{\text{tot}}(\ell)$ is symmetric positive semidefinite,

$$\|\mathbf{J}(\ell)\|_2^2 = \lambda_{\max}(\mathbf{J}(\ell)^\top \mathbf{J}(\ell)) = 1 + \varepsilon^2 \lambda_{\max}(\mathbf{A}_{\text{tot}}(\ell)^\top \mathbf{A}_{\text{tot}}(\ell)).$$

Taking square roots and using $\sqrt{1+x} = 1 + \mathcal{O}(x)$ as $x \rightarrow 0$ yields

$$\|\mathbf{J}(\ell)\|_2 = 1 + \mathcal{O}(\varepsilon^2),$$

which proves the claimed layerwise Jacobian-energy stability. \square

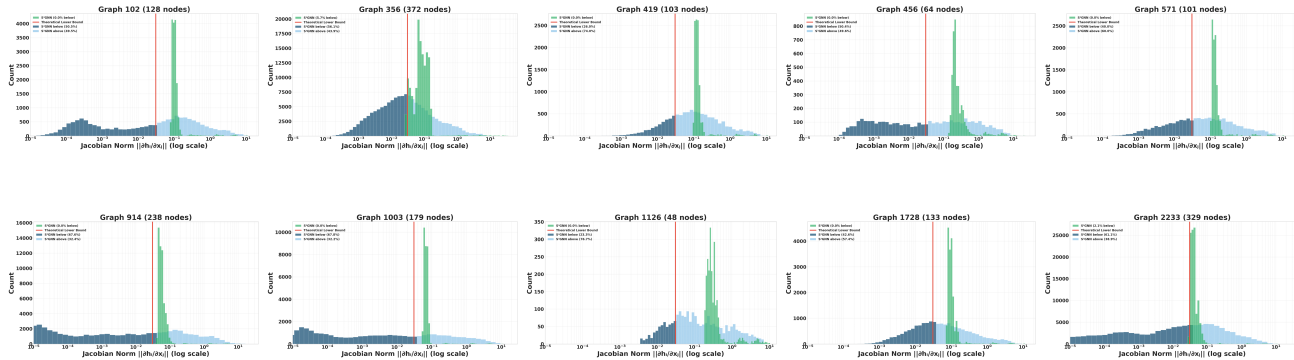


Figure 8. Additional evidence to show the differences in terms of Jacobian norm distributions between three models.

C. Experiment Details and Additional Analysis

C.1. More Evidence on Jacobian Norm Distributions

To enrich the evidence on the Jacobian norm distribution difference between models, i.e., Figure 1, which only shows one sample randomly from the test set. In Figure 8, we additionally plot ten more results with the graph randomly picked up from the test set. These samples are with the node number ranging from 64 to 456. We found that in all plots, S^2GNN 's norm distributions are mixed **below-bound values** and **above-bound values**, whereas S^3GNN s are all above the theoretical lower bounds, except in the graph #356, where we observed around 5.7% of the norms are below the lower bound. These evidence further suggests the violation between the real-implementation and theoretical conclusions, and verifies the effectiveness of our proposed S^3GNN model.

C.2. Baseline Description

We evaluate our proposed model by comparing it to various baselines. For standard graph learning tasks, including graph property prediction, large-scale node classification, and long-range graph learning, our baselines cover a broad spectrum of representative model families.

Graph Property Prediction. For graph-level property prediction tasks, we compare against classical and modern GNN baselines, including GCN (Kipf & Welling, 2016), GAT (Veličković et al., 2018), GraphSAGE (Hamilton et al., 2017), GIN (Xu et al., 2019), GRAND (Chamberlain et al., 2021b), A-DGN (Gravina et al., 2022), ChebNet (Defferrard et al., 2016), Stable-ChebNet (Hariri et al., 2025), DIFFormer (Wu et al., 2023b) and S^2GNN (Geisler et al., 2024).

Node Classification. For large-scale node classification on OGB datasets, we compare against widely used and recent models, including GCN (Kipf & Welling, 2016), ChebNet (Defferrard et al., 2016), ChebNetII (He et al., 2022), GraphSAGE (Hamilton et al., 2017), GAT (Veličković et al., 2018), NodeFormer (Wu et al., 2022), GraphGPS (Rampášek et al., 2022), GOAT (Kong et al., 2023), EXPHORMER+GCN (Shirzad et al., 2023), SPEXPFORMER (Shirzad et al., 2024), DIFFormer (Wu et al., 2023b), and Stable-ChebNet (Hariri et al., 2025).

Long-Range Graph Learning. For long-range graph benchmarks, we include representative baselines from multiple model families. Specifically, we compare with transformer-based models including SAN+LapPE (Kreuzer et al., 2021), TIGT (Choi et al., 2024b), Specformer (Bo et al., 2023), Exphormer (Shirzad et al., 2024), G.MLPMixer (He et al., 2023), and GRIT (Ma et al., 2023); graph rewiring methods including LASER (Barbero et al., 2024) and DRew-GCN (Gutteridge et al., 2023); state-space models including Graph Mamba (Wang et al., 2024) and GMN (Behrouz & Hashemi, 2024).

C.3. Hyperparameter Searching Space

In this section, we provide hyperparameter searching spaces for each of the experiments. Table 8 to 7 summarize the search spaces and the reference hyperparameters. We note that for the experiment in KGQA, topological interpolation, and the fullid dynamic prediction, the hyperparameters for S^3GNN are fixed with step size $\epsilon = 0.1$, Dissipative force $\gamma = 0.01$ and initial $\alpha = 1$, while we keep the rest of the settings exactly the same as the original paper. Please see (Mavromatis & Karypis, 2024; Yang, 2025; Pfaff et al., 2020) for more implementation details.

Table 7. Hyperparameters for LRGB Experiments

Hyperparameter	Peptides-struct	Peptides-func	Search Space
Hidden dimension	256	128	128, 256, 512
Number of Layers	5	7	3, 5, 7
MLP Layers	2	2	1, 2, 3
Batch Size	64	32	32, 64, 128
Learning Rate	0.001	0.001	0.0005, 0.001, 0.005
Step Size (ϵ)	0.5	0.1	0.1, 0.5, 1.0
Initial α	1.0	1.0	1, 2, 3
Dissipation (g)	0.1	0.1	0.01, 0.05, 0.1
Dropout	0.15	0.2	0.1, 0.15, 0.2
Activation	SiLU	SiLU	SiLU, ReLU, tanh
Epochs	200	200	–

Table 8. Hyper-parameter grid for S³GNN on Graph Property Prediction tasks.

Hyper-parameter	Diameter	SSSP	Eccentricity	Search Space
Hidden dim d	40	40	32	32, 40, 96
Num of layers	6	6	12	3, 6, 12, 24
Step size ϵ	0.7	0.1	0.7	0.1, 1.0
Dissipative force γ	0.01	0.01	0.01	0.001, 0.01, 0.05, 0.1
α init	1.0	1.0	1.0	0.5, 1.0, 2.0
Batch size	16	16	16	16, 32, 64
Learning rate	0.001	0.003	0.001	0.001, 0.003, 0.01
Weight decay	10^{-6}	10^{-6}	10^{-6}	10^{-6} , 10^{-5} , 10^{-4}
Epochs	1000	1000	1000	1000

D. Performance on Heterophily Graphs

In this section, we evaluate S³GNN performance on heterophily graphs. We follow the settings in (Behrouz & Hashemi, 2024; Hariri et al., 2025). Specifically, four node classification tasks in the datasets of **Roman-empire**, **Amazon-ratings** and **Minesweeper**, and **Tolokers** are considered. We followed the standard data split for these datasets and the results are presented in Table 10, we note that some of the results are copied based on the online available results (Behrouz & Hashemi, 2024; Hariri et al., 2025). One can see that although with a stronger global mixing effect than classic GCN, causing better information transaction, S³GNN still shows state-of-the-art results for all datasets.

Table 9. Hyperparameters for OGB Node Classification Experiments

Hyper-parameter	OGBN-Proteins	OGBN-ArXiv	Search Space
Hidden Channels	256	256	128, 256, 512, 1024
Number of Layers	10	5	2, 3, 4, 5, 7, 10
Step Size (ϵ)	0.1	0.1	0.1, 1.0
Dissipation (g)	0.1	0.1	0.01, 0.05, 0.1
Initial α	1.0	1.0	1, 2, 3
Learning Rate	0.001	0.001	0.0005, 0.001, 0.005, 0.01
Batch Size	1024	1024	256, 512, 1024
Dropout	0.1	0.2	0.1,0.2,0.3
Activation	tanh	ReLU	tanh, ReLU

Table 10. Mean test set score and std averaged over 4 random weight initializations on heterophilic datasets. The higher, the better.

Model	Roman-empire Acc \uparrow	Amazon-ratings Acc \uparrow	Minesweeper AUC \uparrow	Tolokers AUC \uparrow
MLP-2	66.04 \pm 0.71	49.55 \pm 0.81	50.92 \pm 1.25	74.58 \pm 0.75
SGC-1	44.60 \pm 0.52	40.69 \pm 0.42	82.04 \pm 0.77	73.80 \pm 1.35
MLP-1	64.12 \pm 0.61	38.60 \pm 0.41	50.59 \pm 0.83	71.89 \pm 0.82
MPNNs				
GAT	80.87 \pm 0.30	49.09 \pm 0.63	92.01 \pm 0.68	83.70 \pm 0.47
GAT (LapPE)	84.80 \pm 0.46	44.90 \pm 0.73	93.50 \pm 0.54	84.99 \pm 0.54
GAT (RWSE)	86.62 \pm 0.53	48.58 \pm 0.41	92.53 \pm 0.65	85.02 \pm 0.67
Gated-GCN	74.46 \pm 0.54	43.00 \pm 0.32	87.54 \pm 1.22	77.31 \pm 1.14
GCN	73.69 \pm 0.74	48.70 \pm 0.63	89.75 \pm 0.52	83.64 \pm 0.67
GCN (LapPE)	83.37 \pm 0.55	44.35 \pm 0.36	94.26 \pm 0.49	84.95 \pm 0.78
GCN (RWSE)	84.84 \pm 0.55	46.40 \pm 0.55	93.84 \pm 0.48	85.11 \pm 0.77
CO-GNN(Σ, Σ)	91.57 \pm 0.32	51.28 \pm 0.56	95.09 \pm 1.18	83.36 \pm 0.89
CO-GNN(μ, μ)	91.37 \pm 0.35	54.17 \pm 0.37	97.31 \pm 0.41	84.45 \pm 1.17
SAGE	85.74 \pm 0.67	53.63 \pm 0.39	93.51 \pm 0.57	82.43 \pm 0.44
Graph Transformers				
Expformer	89.03 \pm 0.37	53.51 \pm 0.46	90.74 \pm 0.53	83.77 \pm 0.78
NAGphormer	74.34 \pm 0.77	51.26 \pm 0.72	84.19 \pm 0.66	78.32 \pm 0.95
GOAT	71.59 \pm 1.25	44.61 \pm 0.50	81.09 \pm 1.02	83.11 \pm 1.04
GPS	82.00 \pm 0.61	53.10 \pm 0.42	90.63 \pm 0.67	83.71 \pm 0.48
GPS _{GCN} +Performer (LapPE)	83.96 \pm 0.53	48.20 \pm 0.67	93.85 \pm 0.41	84.72 \pm 0.77
GPS _{GCN} +Performer (RWSE)	84.72 \pm 0.65	48.08 \pm 0.85	92.88 \pm 0.50	84.81 \pm 0.86
GT	86.51 \pm 0.73	51.17 \pm 0.66	91.85 \pm 0.76	83.23 \pm 0.64
GT-sep	87.32 \pm 0.39	52.18 \pm 0.80	92.29 \pm 0.47	82.52 \pm 0.92
Polynomial	92.55 \pm 0.30	54.81 \pm 0.49	97.46 \pm 0.36	85.91 \pm 0.74
Heterophily-Designated GNNs				
CPGNN	63.96 \pm 0.62	39.79 \pm 0.77	52.03 \pm 5.46	73.36 \pm 1.01
FAGCN	65.22 \pm 0.56	44.12 \pm 0.30	88.17 \pm 0.73	77.75 \pm 1.05
FSGNN	79.92 \pm 0.56	52.74 \pm 0.83	90.08 \pm 0.70	82.76 \pm 0.61
GBK-GNN	74.57 \pm 0.47	45.98 \pm 0.71	90.85 \pm 0.58	81.01 \pm 0.67
GloGNN	59.63 \pm 0.69	36.89 \pm 0.14	51.08 \pm 1.23	73.39 \pm 1.17
GPR-GNN	64.85 \pm 0.27	44.88 \pm 0.34	86.24 \pm 0.61	72.94 \pm 0.97
H2GCN	60.11 \pm 0.52	36.47 \pm 0.23	89.71 \pm 0.31	73.35 \pm 1.01
JacobiConv	71.14 \pm 0.42	43.55 \pm 0.48	89.66 \pm 0.40	68.66 \pm 0.65
Graph SSMs				
GMN	87.69 \pm 0.50	54.07 \pm 0.31	91.01 \pm 0.23	84.52 \pm 0.21
GPS + Mamba	83.10 \pm 0.28	45.13 \pm 0.97	89.93 \pm 0.54	83.70 \pm 1.05
GRAMA _{GCN}	88.61 \pm 0.43	53.48 \pm 0.62	95.27 \pm 0.71	86.23 \pm 1.10
MP-SSM	90.91 \pm 0.48	53.65 \pm 0.71	95.33 \pm 0.72	85.26 \pm 0.93
S ³ GNN(ours)	91.52 \pm 0.15	53.46 \pm 0.70	97.58 \pm 0.44	85.89 \pm 1.05